



**HAL**  
open science

## Three-dimensional direct numerical simulations of the dynamics of retracting surfactant-laden ligaments

Cristian R. Constante-Amores, Lyes Kahouadji, Assen Batchvarov, Omar K. Matar, Seungwon Shin, Jalel Chergui, Damir Juric

► **To cite this version:**

Cristian R. Constante-Amores, Lyes Kahouadji, Assen Batchvarov, Omar K. Matar, Seungwon Shin, et al.. Three-dimensional direct numerical simulations of the dynamics of retracting surfactant-laden ligaments. *Physical Review Fluids*, 2020, 5, pp.084007. 10.1103/PhysRevFluids.5.084007. hal-02610695v1

**HAL Id: hal-02610695**

**<https://hal.science/hal-02610695v1>**

Submitted on 26 May 2020 (v1), last revised 24 Jan 2023 (v2)

**HAL** is a multi-disciplinary open access archive for the deposit and dissemination of scientific research documents, whether they are published or not. The documents may come from teaching and research institutions in France or abroad, or from public or private research centers.

L'archive ouverte pluridisciplinaire **HAL**, est destinée au dépôt et à la diffusion de documents scientifiques de niveau recherche, publiés ou non, émanant des établissements d'enseignement et de recherche français ou étrangers, des laboratoires publics ou privés.

# Three-dimensional direct numerical simulations of the dynamics of retracting surfactant-laden ligaments

R. Constante-Amores, L. Kahouadji,\* A. Batchvarov, and O. K. Matar  
*Department of Chemical Engineering, Imperial College London,  
South Kensington Campus, London SW7 2AZ, United Kingdom*

S. Shin  
*Department of Mechanical and System Design Engineering,  
Hongik University, Seoul 121-791, Republic of Korea*

J. Chergui and D. Juric  
*Laboratoire d'Informatique pour la Mécanique et les Sciences de l'Ingénieur (LIMSI),  
Centre National de la Recherche Scientifique (CNRS), Université Paris Saclay,  
Bât. 507, Rue du Belvédère, Campus Universitaire, 91405 Orsay, France*  
(Dated: January 31, 2020)

The dynamics of ligaments retracting under the action of surface tension occurs in a multitude of natural and industrial applications, such as inkjet printing and atomisation. We perform fully three-dimensional, two-phase direct numerical simulations of the retraction dynamics with soluble surfactants. A full parametric study is performed using a hybrid interface-tracking/level-set method, which is utilised to treat the interface; this method is capable of capturing faithfully the topological transitions that are a feature of the flow over a certain range of ligament aspect ratios and Ohnesorge numbers. Our results demonstrate the delicate interplay between capillarity, modulated by the presence of surfactants, surfactant-induced Marangoni stresses, inertial and viscous effects. Particular attention is paid to the formation of vortices, which accompany the retraction process, and the influence of surfactant on the vortex dynamics.

arXiv:2001.11029v1 [physics.flu-dyn] 29 Jan 2020

---

\* l.kahouadji@imperial.ac.uk

## I. INTRODUCTION

Fluid ligaments undergo a surface tension-driven instability if their lengths exceeds their perimeter [27, 29] or retraction into a single spherical drop or a multitude of droplets, in order to minimise interfacial energy. These phenomena are observed in multiple applications, such as, for instance, atomisation or spray formation [11, 22], ink-jet printing or micro-encapsulation [3, 9, 13]. In the absence of surfactant, the retracting dynamics of a Newtonian liquid thread surrounded by a passive ambient gas has been studied by Schulkes [30], and Notz and Basaran [26] using a Galerkin finite element approach under a two-dimensional axisymmetric assumption in the azimuthal direction, and by also assuming another symmetry through the ligament mid-plane in the longitudinal direction; the flow is parameterised by the ligament aspect ratio,  $L_o = L/R$ , and Ohnesorge number,  $Oh = \mu/\sqrt{\rho\sigma R}$ , where  $L$  and  $R$  are the initial length and radius of the ligament, while  $\rho$ ,  $\mu$ , and  $\sigma$  are the density, dynamic viscosity, and surface tension, respectively.

Schulkes [30] has simulated the ligament retraction towards a minimum radius of  $r \sim 0.8R$ , where  $r$  is the radial coordinate, while Notz and Basaran [26] were able to reach  $r \sim 10^{-4} \times R$ . Notz and Basaran [26] have also presented the temporal evolution of a retracting ligament of aspect ratio  $L_o = 15$  for three different regimes depending on the magnitude of  $Oh$ : (i) low  $Oh$  values ( $Oh \sim 10^{-3}$ ), where capillarity is more dominant than viscous forces, the outcome is the formation of two bulbous regions at both ends of the ligament that pinchoff eventually leading to the formation of a smaller, secondary ligament; (ii) intermediate  $Oh$  values ( $Oh \sim 10^{-2}$ ), where there is a balance between viscous and capillary forces, a situation that culminates in the breakup of the ligament into three droplets; (iii) at higher  $Oh$  values ( $Oh \sim 10^{-1}$ ), which reflects the dominance of viscous forces and for which the retraction is not accompanied by breakup but by the formation of a single spherical drop.

Notz and Basaran [26] have also presented a detailed regime map of the ligament evolution prior to breakup, varying both  $L_o$  and  $Oh$ . Castrejon-Pita *et al.* [4] performed experiments on retracting ligaments beyond breakup, and, more recently, Anthoni *et al.* [1] extended the work of Notz and Basaran [26], considering all possible ranges of fluid properties ( $Oh = 10^{-3} - 10^0$ ) and aspect ratios ( $L_o = 5 - 10^3$ ). The studies summarised in the foregoing have shown that the ligament dynamics are characterised a longitudinal retraction followed by one or possibly several breakups events which lead to satellite droplet formation. The presence of surface-active chemicals in the retracting ligament, either as an additive or a contaminant, could, potentially, have a strong influence on the emergent dynamics. This has not received as much attention as the surfactant-free case, and is the subject of the present paper.

It is well known through the work of Eggers [10] that the breakup of a liquid thread follows a self-similar behaviour as rupture is approached. Craster *et al.* [5] showed that the presence of surfactant does not alter the breakup scalings; this is because the surfactant is convected away from the thread 'neck' under the action of surface tension that drives fluid away from that region. Xu [40] studied numerically the effect of insoluble surfactant on the recoiling filament under similar symmetry assumptions to those adopted by Notz and Basaran [26] for multiple values of  $Oh$ . McGough and Basaran [23] carried out computational studies in order to observe the formation of successive surfactant-covered threads. More recently, Kamal *et al.* [20] performed both experiments and numerical simulations of Newtonian pendant droplets covered by insoluble surfactants using doubly-axisymmetric simulations, and Wang *et al.* [41] have performed both experimental and two-dimensional axisymmetric computations to determine the influence of capillary waves on the ligament stability. Dziejczak *et al.* [8] have also studied the dynamics of ligaments including substrate effects; here, only a quarter of the ligament was modelled through the use of symmetry conditions.

Despite the attention received by ligament dynamics in the literature, the effect of surfactant, and associated surfactant-induced Marangoni stresses, on the three-dimensional (3D) evolution of the ligament has not yet been reported. The aim of the present paper is therefore to perform 3D numerical simulations of the retraction process over a wide range of system parameters that account for surfactant solubility and sorption kinetics, bulk and interfacial diffusion, and Marangoni stresses. We will consider situations characterised by ligament pinchoff, and attention will be paid to the formation of vortical structures during the flow evolution. The results will be used to elucidate the mechanisms underlying the flow phenomena observed to accompany the dynamics.

The rest of this article is organized as follows. Section II presents the governing equations for the flow and surfactant transport, the simulation configuration, and the numerical methods. In Section III, we present a discussion of our results focusing on the effect of surfactant on the dynamics of the thread, a parametric study with respect to the governing surfactant parameters, and a detailed analysis of the vorticity. Finally, concluding remarks are provided in Section IV.

## II. PROBLEM FORMULATION AND NUMERICAL METHODS

In this section, we provide the main steps in the problem formulation together with details of the hybrid interface-tracking/level-set approach to treat the interface. As presented in Fig. 1-(a), we consider an initially axisymmetric

cylinder terminated by hemispherical caps at its two ends and surrounded by a gas phase. The governing equations for incompressible and immiscible two-phase fluid systems in a three-dimensional Cartesian domain  $\mathbf{x} = (x, y, z)$  are expressed by a single field formulation for the continuity and the momentum balance equation:

$$\nabla \cdot \mathbf{u} = 0, \quad (1)$$

$$\rho \left( \frac{\partial \mathbf{u}}{\partial t} + \mathbf{u} \cdot \nabla \mathbf{u} \right) = -\nabla p + \nabla \cdot \mu (\nabla \mathbf{u} + \nabla \mathbf{u}^T) + \mathbf{F}, \quad (2)$$

where  $\mathbf{u}$  stands for the velocity,  $p$  for the pressure, and  $t$  denotes time. The density  $\rho$  and dynamic viscosity  $\mu$  are given by

$$\begin{aligned} \rho(\mathbf{x}, t) &= \rho_g + (\rho_l - \rho_g) I(\mathbf{x}, t), \\ \mu(\mathbf{x}, t) &= \mu_g + (\mu_l - \mu_g) I(\mathbf{x}, t), \end{aligned} \quad (3)$$

using a single-field formulation in which  $I$  represents a Heaviside function, while the ‘g’ and ‘l’ subscripts designate the gas and liquid-phase quantities, respectively. The last term in (2) represents the surface tension force, which is decomposed into its normal component ( $\mathbf{F}_n$ ) for the normal stress jump across the interface, and its tangential component ( $\mathbf{F}_s$ ), which is associated with the surface gradient of the surface tension [31],  $\nabla_s \sigma$ :

$$\mathbf{F} = \mathbf{F}_n + \mathbf{F}_s = \int_{A(t)} \sigma \kappa \mathbf{n} \delta(\mathbf{x} - \mathbf{x}_f) dA + \int_{A(t)} \nabla_s \sigma \delta(\mathbf{x} - \mathbf{x}_f) dA. \quad (4)$$

Here,  $\kappa$  and  $\mathbf{n}$  denote the curvature and the outward-pointing unit normal, respectively, and the surface gradient operator is given by  $\nabla_s = [\mathbf{I} - \mathbf{nn}] \cdot \nabla$  wherein  $\mathbf{I}$  is the identity tensor. In these formulae,  $\mathbf{x}_f$  is an interface parameterisation,  $A(t)$ , and  $\delta(\mathbf{x} - \mathbf{x}_f)$  is a Dirac distribution that is non-zero only when  $\mathbf{x} = \mathbf{x}_f$ . We use a hybrid front-tracking/level-set technique (also known as Level Contour Reconstruction Method, LCRM) proposed by Shin and Juric [31, 32, 35] to predict the location of the interface. The LCRM is capable of predicting accurately  $\mathbf{F}_n$  and  $\mathbf{F}_s$  and of handling deforming interfaces with topological changes. The solver follows a decomposition strategy for its parallelization with a message-passing-interface algorithm; further details of the numerical method can be found in the work of Shin *et al.* [33]

In addition to the equations of motion given above, the set of convection-diffusion equations describing the transport of surfactant species in the bulk and on the interface, with concentrations  $C$  and  $\Gamma$ , respectively, are expressed by

$$\frac{\partial C}{\partial t} + \mathbf{u} \cdot \nabla C = \nabla \cdot (D_c \nabla C), \quad (5)$$

and

$$\frac{\partial \Gamma}{\partial t} + \nabla_s \cdot (\Gamma \mathbf{u}_t) = D_s \nabla_s^2 \Gamma + J, \quad (6)$$

where  $\mathbf{u}_t = (\mathbf{u}_s \cdot \mathbf{t}) \mathbf{t}$  is the tangential velocity on the interface in which  $\mathbf{u}_s$  represents the surface velocity;  $D_s$  and  $D_c$  denote the surfactant interfacial and bulk diffusivities, respectively, and  $J$  is the sorptive flux, which provides a relationship between  $C$  and  $\Gamma$  that connects the bulk and interfacial concentrations. The left-hand-side of Eq. (6) represents the transient and convective transport of surfactant at the interface, and its right-hand side models interfacial diffusion and bulk-interface mass exchange. The flux  $J$  is expressed by

$$J = k_a C_s (\Gamma_\infty - \Gamma) - k_d \Gamma, \quad (7)$$

where  $k_a$  and  $k_d$  stand for the kinetic constants for adsorption and desorption, respectively, and  $C_s$  denotes the surfactant concentration in the sub-phase adjoining the interface.

The equation of state describing the variation of the surface tension as a function of the local interfacial surfactant concentration is given by the Langmuir relation [31]

$$\sigma(\Gamma) = \sigma_s + RT \Gamma_\infty \ln \left( 1 - \frac{\Gamma}{\Gamma_\infty} \right), \quad (8)$$

where  $\sigma_s$  is the surface tension in the absence of surfactant, and  $\Gamma_\infty$  is interfacial concentration at maximal packing.

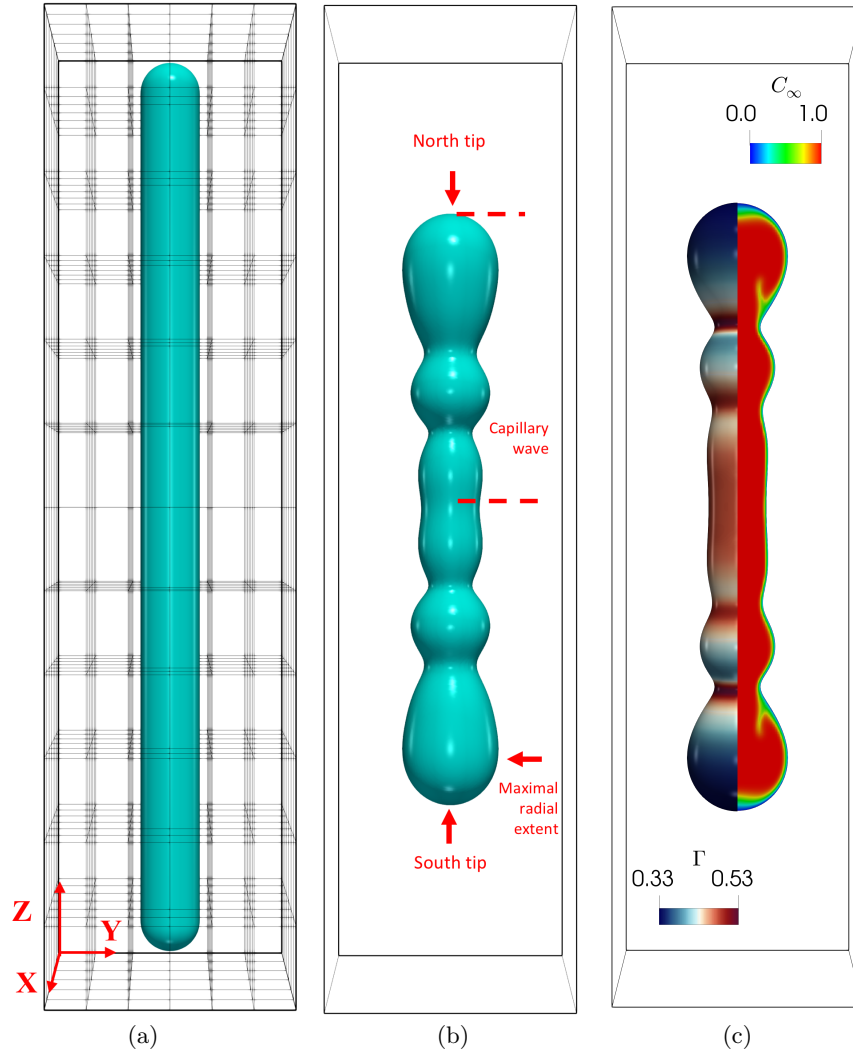


FIG. 1: Initial shape of the ligament, (a), highlighting the computational domain of size  $8R \times 8R \times 32R$  in a three-dimensional Cartesian domain  $\mathbf{x} = (x, y, z)$  and divided into  $6 \times 6 \times 12$  sub-domains; the Cartesian resolution is set to  $32 \times 32 \times 64$  per sub-domain, and the global resolution is  $192 \times 192 \times 768$ . Typical interfacial shape for a surfactant-free case at  $t = 7$  for  $L_o = 15$  and  $Oh = 10^{-2}$ , (b), with definitions of particular locations and features whose dynamics will be discussed in the present work. Typical interfacial shape for a surfactant-laden case at  $t = 7$  with  $L_o = 15$ ,  $Oh = 10^{-2}$ ,  $Bi = 1$ ,  $Pe = 10$ , and  $x = 0.9$  with colour bars indicating the magnitude of the surfactant interfacial and bulk concentrations in the left and right halves of the ligament, respectively.

All variables are rendered non-dimensional by using the following scaling where the tildes designate dimensionless quantities:

$$\tilde{r} = \frac{r}{R}, \quad \tilde{t} = \frac{t}{t_R}, \quad \tilde{\mathbf{u}} = \frac{\mathbf{u}}{u_R}, \quad \tilde{p} = \frac{p}{\rho_l u_R^2}, \quad \tilde{\rho} = \frac{\rho}{\rho_l}, \quad \tilde{\mu} = \frac{\mu}{\mu_l}, \quad \tilde{\sigma} = \frac{\sigma}{\sigma_s}, \quad \tilde{\Gamma} = \frac{\Gamma}{\Gamma_\infty}, \quad \tilde{C} = \frac{C}{C_\infty}, \quad (9)$$

here,  $t_R = \sqrt{\rho_l R^3 / \sigma_s}$  corresponds to the capillary time scale and  $C_\infty$  the bulk concentration. Hence, velocities are scaled on the capillary velocity  $u_R = R/t_r = \sqrt{\sigma_s / (\rho_l R)}$ . As a result of this scaling, Eqs. (1)-(8) become

$$\nabla \cdot \tilde{\mathbf{u}} = 0, \quad (10)$$

$$\tilde{\rho} \left( \frac{\partial \tilde{\mathbf{u}}}{\partial \tilde{t}} + \tilde{\mathbf{u}} \cdot \nabla \tilde{\mathbf{u}} \right) + \nabla \tilde{p} = Oh \nabla \cdot \left[ \tilde{\mu} (\nabla \tilde{\mathbf{u}} + \nabla \tilde{\mathbf{u}}^T) \right] + \int_{\tilde{A}(\tilde{t})} \tilde{\sigma} \tilde{\kappa} \mathbf{n} \delta(\tilde{\mathbf{x}} - \tilde{\mathbf{x}}_f) d\tilde{A} + \int_{\tilde{A}(\tilde{t})} \nabla_s \tilde{\sigma} d\tilde{A}, \quad (11)$$

$$\frac{\partial \tilde{C}}{\partial \tilde{t}} + \tilde{\mathbf{u}} \cdot \nabla \tilde{C} = \frac{1}{Pe_b} \nabla \cdot (\nabla \tilde{C}), \quad (12)$$

$$\frac{\partial \tilde{\Gamma}}{\partial \tilde{t}} + \nabla_s \cdot (\tilde{\Gamma} \tilde{\mathbf{u}}_t) = \frac{1}{Pe_s} \nabla_s^2 \tilde{\Gamma} + \tilde{J}, \quad (13)$$

$$\tilde{J} = Bi \left( k \tilde{C} (1 - \tilde{\Gamma}) - \tilde{\Gamma} \right), \quad (14)$$

$$\tilde{\sigma} = 1 + \beta_s \ln(1 - \tilde{\Gamma}), \quad (15)$$

in which the dimensionless parameters appearing in these equations are given by

$$Oh = \frac{\mu_l}{\sqrt{\rho_l \sigma_s R}}, \quad Bi = k_d R \sqrt{\frac{\rho_l R}{\sigma_s}}, \quad \beta_s = \frac{RT \Gamma_\infty}{\sigma_s}, \quad Pe_b = \frac{1}{D_b} \sqrt{\frac{\sigma_s R}{\rho_l}}, \quad \text{and} \quad Pe_s = \frac{1}{D_s} \sqrt{\frac{\sigma_s R}{\rho_l}}. \quad (16)$$

where  $Oh$  denotes the Ohnesorge number and measures the relative importance of viscous to surface tension forces,  $Bi$  is the Biot number representing the ratio of characteristic desorptive to convective time-scales,  $\beta_s$  is the elasticity number, which measures the sensitivity of the surface tension to changes in surfactant interfacial concentration;  $Pe_s$  and  $Pe_b$  are the interfacial and bulk Peclet numbers and compare the ratio of convective to diffusive time-scales in the plane of the interface and the bulk, respectively. The viscosity and density ratios are represented by  $\rho_g/\rho_l$  and  $\mu_g/\mu_l$  and they correspond to  $1.2 \times 10^{-3}$  and  $1.8 \times 10^{-2}$  respectively, corresponding to a water ligament in air.

At equilibrium, the equation (7) reduces to the Langmuir adsorption isotherm

$$x = \frac{\Gamma_{eq}}{\Gamma_\infty} = \frac{k}{1+k}, \quad k = \frac{k_a C_\infty}{k_d}, \quad (17)$$

where  $x$  stands for the fraction of surface covered by adsorbed surfactant,  $k$  is the adsorption parameter, which represents the ratio of adsorption to desorption time scales. Finally, the Marangoni stress  $\nabla_s \sigma$  due to the presence of surfactant is expressed in terms of gradients in  $\Gamma$  as follows:

$$\nabla_s \tilde{\sigma} = -\frac{\beta_s}{1 - \tilde{\Gamma}} \nabla_s \tilde{\Gamma} \quad (18)$$

For simplicity, the tildes are dropped henceforth.

The time scale associated with the Marangoni flow is determined from a balance between Marangoni stresses and viscous retardation,  $\nabla_s \sigma \sim \Delta \sigma / R \sim \mu_l / t_M$ , hence  $t_M = \mu_l R / \Delta \sigma$ , and it is of order  $10^{-3}$  s. However, the capillary breakup time is of order  $10^{-2}$  s, and the time scale associated with the retraction of the ligament is also of order  $10^{-2}$  s. For the soluble cases, we consider the properties of n-alcohols (such as n-propanol, n-butanol and n-pentanol) or dicarboxylic acid type (such as adipic and pimelic acid) as surfactants, which are characterised by desorptive time scales of  $10^{-2}$  s [2, 15, 16]. Therefore, for both soluble and insoluble surfactant configuration, Marangoni stress will play a major role in the ligament retraction dynamics.

As introduced in the beginning of this section, the liquid ligament is initialised as a cylindrical thread in the centre of the domain with hemispherical caps at its two edges (see Fig. 1-a). The aspect ratio of the liquid thread fixed as  $L_o = 15$  and the size of the three-dimensional computation domain is  $8R \times 8R \times 32R$ . An example of the interface position, together with definitions of particular features and locations on the ligament surface to which reference will be made below, are shown in Fig. 1-(b). Also shown in this figure is the partitioning of the computational domain into subdomains for deployment of the MPI decomposition technique for code parallelisation. Numerical solutions are obtained subject to Dirichlet boundary conditions on the velocity and Neumann conditions on the pressure. Both soluble and insoluble surfactants are considered in this study and numerical simulations are arranged into three groups. The first group is focused on the effect of insoluble surfactant on the interfacial dynamics of the interface for which  $Pe_s$  is varied with  $\beta_s = 0.3$  held constant. The second group of simulations was launched to study the effect of Marangoni stresses for which  $\beta_s$  is varied with  $Pe_s = 10$  held constant. Finally, the last set of numerical simulations has the objective to understand the surfactant mass transfer between the interface and the bulk.

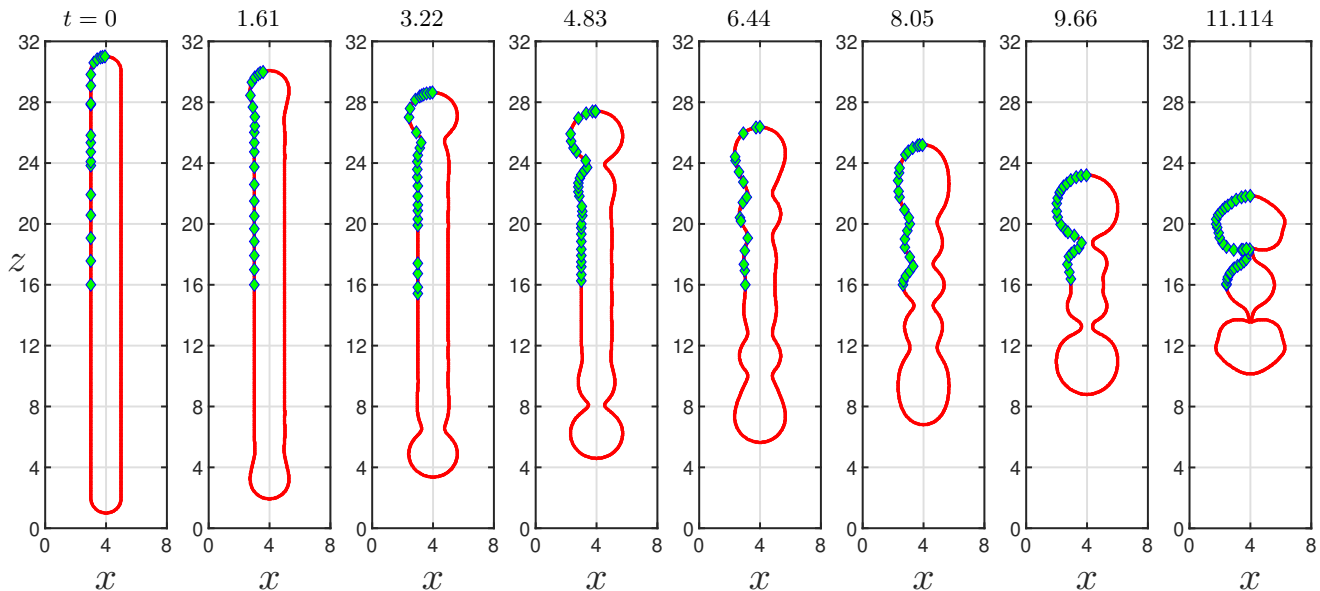


FIG. 2: Spatio-temporal evolution of a retracting ligament for  $L_o = 15$  and  $Oh = 10^{-2}$ . The solid lines correspond to the results of the present study and the diamonds are collected from Notz and Basaran [26].

### III. RESULTS

In this section, we present a discussion of our results, beginning by comparing our predictions with previous work on retracting surfactant-free ligaments. This serves the purpose of validating our numerical method and provides a benchmark against which to highlight the effects associated with the presence of surfactant.

#### A. Surfactant-free ligament retraction and breakup

We study the retraction of a surfactant-free ligament with  $L_o = 15$  and  $Oh = 10^{-2}$  previously examined by Schulkes [30] and Notz and Basaran [26] paying particular attention to interfacial breakup and post-pinchoff dynamics. In order to inspire confidence in the reliability of the numerical method used to carry out the computations, we show in Fig. 2 a comparison between our numerical predictions and those from the Notz and Basaran [26] which reveals excellent agreement. Fig. 3 depicts time-space plots of the interface, pressure, and the axial velocity; for the latter two, spatial variations are shown with respect to the ligament centreline. The initially motionless, cylindrical ligament undergoes retraction due to the pressure gradient between the two bulbous ends and the rest of the ligament, which drives flow from these regions towards its centre in the form of a capillary wave; this dominates the early stages of the dynamics.

The retraction velocity results from a force balance between capillary and inertial forces, the latter being proportional to the rate of change of momentum of the bulbous ends. Extending the Taylor-Culick expression for the retraction of a two-dimensional axisymmetric planar liquid sheet to a cylindrical thread, we arrive at  $V = (2\sigma_s/\rho_l\pi R)^{1/2}$ , which gives a value for the vertical velocity of retraction 0.079 m/s. This is in good agreement with the retraction velocity predicted by our simulations,  $\sim 0.0789$  m/s and provides further validation of the accuracy and reliability of our numerical method.

The retraction motion and associated capillary waves form neck regions near the two ends of the ligament connecting the bulbous regions with the rest of the ligament. The pressure under these neck regions is large and drives flow away from this region on time scales shorter than those related to retraction, dominating the intermediate stage of the dynamics, and promoting further necking and an even larger pressure gradient that eventually leads to a double pinchoff event for the set of parameters used to generate these results; the profiles for the interface, pressure, and axial velocity associated with this event are highlighted in red in Fig. 3-(d) and (f).

Fig. 3-(a), which highlights the temporal evolution of the north and south tips of the bulbous ligament ends during retraction, also shows that the pinchoff, which takes place at  $t \sim 11.11$ , is followed by the formation of three droplets (see Fig. 3-(a) for  $t = 11.4$ ). These droplets are sufficiently close that a double coalescence takes place at  $t = 12.1$  generating capillary waves that travel up and down the ligament (see 3-(a) for  $t = 12.6, 14,$  and  $15.2$ ). These waves

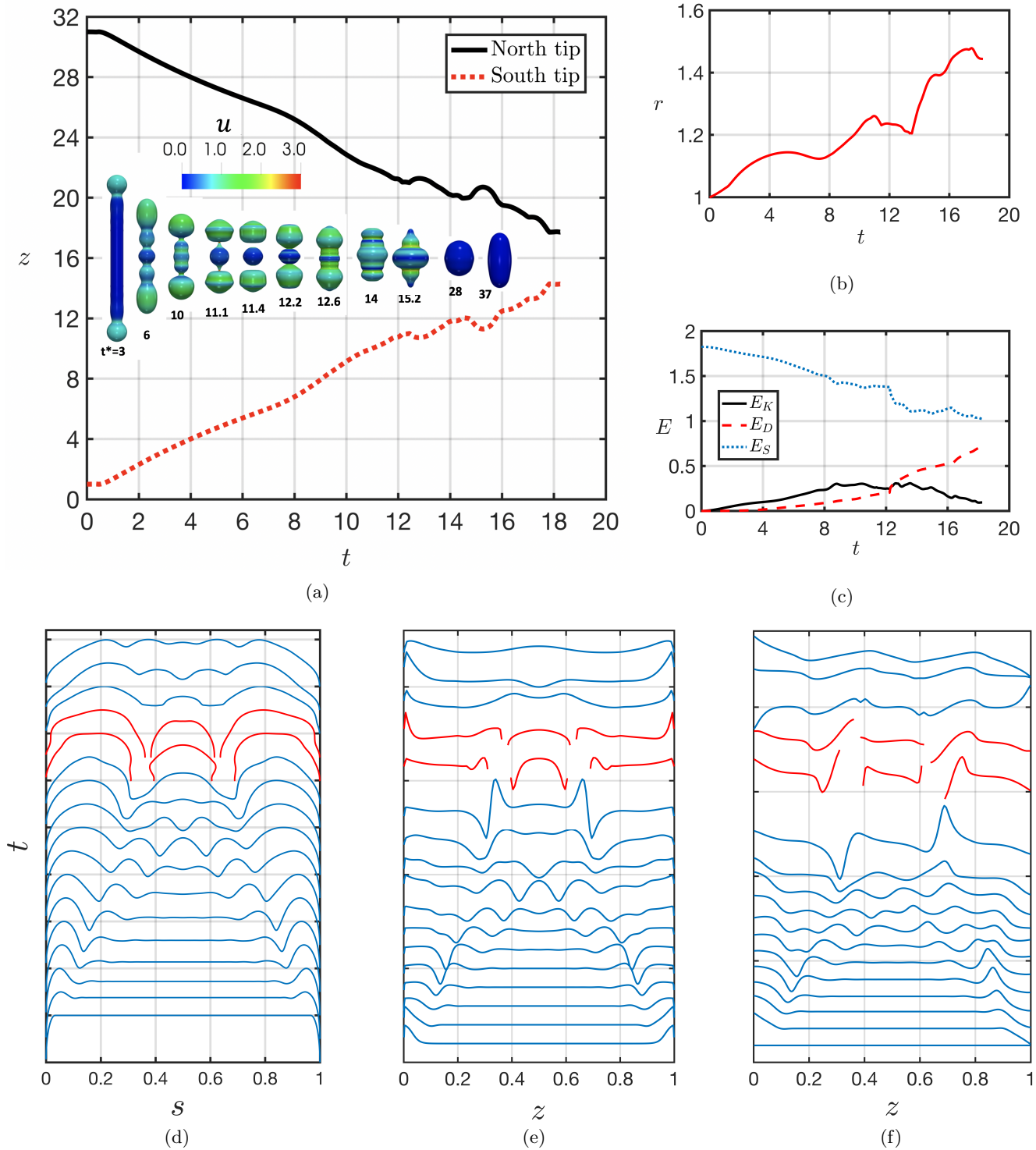


FIG. 3: Surfactant-free ligament retraction for  $L_o = 15$  and  $Oh = 10^{-2}$ : (a) Temporal evolution of the location of both ligament tips, and a three-dimensional representation of the interface for the dimensionless times shown in the panel in which the colour bar depicts the velocity magnitude; (b) temporal evolution of the maximal radial extent of the ligament; and (c) temporal evolution of the kinetic and surface energies,  $E_K$  and  $E_S$ , respectively, and the energy dissipated,  $E_D$ ; (d)-(f) time-space plots of the interface,  $p$ , and  $u_z$ , respectively, with snapshots shown between  $t = 0 - 13.5$ , with time intervals of 1 between  $t = 0 - 11$  and 0.5 between  $t = 11 - 13.5$ ; here, the red profiles are associated with  $t = 11.5$  and  $t = 12$ , the instances at which pinchoff occurs.

decelerate giving way to decaying oscillations between a spherical and an ellipsoidal ligament shape that are the main features of the late-time dynamics (see 3-(a) for  $t = 28$  and 37).

It is also instructive to perform an analysis of the temporal variation of the system energy. The total energy must be constant over time and its constituents are the surface energy,  $E_s = S\sigma_s$ , where  $S$  is the superficial area of the ligament, the kinetic energy,  $E_k = 1/2(u^2 + v^2 + w^2)$ , and the energy dissipated,  $E_D$ . As highlighted in Fig. 3-(c), all energies are normalised by the surface energy of a motionless spherical droplet with a volume similar to that of the ligament of aspect ratio  $L_o = 15$ . Initially, the total energy is represented by the surface energy  $E_s$  solely. When the ligament retracts, part of the surface energy is transferred into kinetic energy. During the coalescence of the three droplets ( $t \sim 12.1$ ) the total area of the system significantly and a fraction of the surface energy is transferred into dissipation energy (see Fig. 3-(c)). At longer times,  $E_s \rightarrow 1$  and  $E_k \rightarrow 0$ , as the ligament tends towards a steady, spherical shape.

### B. Surfactant-laden ligament retraction: insoluble surfactant case

In this section, we present the effect of insoluble surfactant on the dynamics of a retracting ligament with  $L_o = 15$ ,  $Oh = 10^{-2}$ ,  $Pe_s = 10$ ,  $\beta_s = 0.3$ , and  $\Gamma_o = \Gamma_\infty/2$ . Fig. 4 depicts the spatio-temporal evolution of the interface and  $\Gamma$  together with the pressure and axial velocity along ligament centreline. Similar to the surfactant-free case, retraction is accompanied by the formation of capillary waves that dominate the dynamics leading to the collapse of the initially-cylindrical ligament towards a spherical one. The surfactant concentration  $\Gamma$  is coupled to the interfacial dynamics through the dependence of  $\sigma$  on  $\Gamma$ , is redistributed along the interface, and achieves a maximal value around  $t \sim 15$  since the ligament area decreases as it approaches a spherical shape. As shown clearly in Fig. 4-(a) and (b), the presence of surfactant retards ligament retraction as evidenced by the slower temporal evolution of the ligament tips and lower kinetic energy in comparison to the surfactant-free case; the retraction speed is  $\sim 0.070$  m/s as compared to  $\sim 0.0789$  m/s in the ‘clean’ case. This is due to the surfactant-induced interfacial rigidification brought about by the Marangoni stresses, which, in turn, are caused by gradients in  $\Gamma$ .

In order to elucidate the coupling between interface and surfactant concentration, we consider the interface,  $\Gamma$ ,  $p$ , and  $u_z$ , at  $t = 10$  shown in red dashed lines panels (c)-(f) of Fig. 4. The retraction capillary waves are characterised by regions of radially-diverging and converging motion and associated higher and lower interfacial areas and therefore reduced (increased) and increased (reduced)  $\Gamma$  ( $\sigma$ ) locally, respectively. These concentration gradients lead to Marangoni stresses that drive flow from the higher-tension radially-diverging to the lower-tension converging regions, which act to retard the interfacial motion. To further illustrate the retarding effect of the Marangoni stresses, three distinct regions are also highlighted, as shown in Fig. 5-(a). In Region ‘A’, the interfacial flow diverges away from point ‘1’, at the ligament tip, driving surfactant away from this location leading to the lowest  $\Gamma$  value along the interface. There is an overall increase in  $\Gamma$  from the tip towards the centre reaching a maximal value at location ‘3’ at which the interface exhibits a local minimum. The  $\Gamma$  profile then undergoes oscillations in response to the wavy shape of the interface, with a local minimum and maximum in  $\Gamma$  at locations ‘4’ and ‘5’ that coincide with a local interfacial maximum and minimum, respectively. It is clear from Fig. 5-(a) that  $\nabla_s \sigma < 0$  in Region A suggesting that the direction of the Marangoni flow is towards the ligament tip, which acts to retard the capillary-driven flow from the tip towards the centre; this retarding effect in Region A manifests itself through a decrease in the tangential velocity along the interface,  $u_t$ , as shown in Fig. 5-(b). In Region B,  $\nabla_s \sigma > 0$ , thus Marangoni-driven flow is towards the ligament centre, which is counter to the capillary flow away from this necking region. As also indicated in Fig. 5-(b),  $u_t$ , which was negative in Region B in the surfactant-free, becomes positive in the surfactant-laden case. Finally, it is also evident that using similar mechanisms, the Marangoni-driven flow reduces substantially the magnitude of  $u_t$  in Region C. Fig. 5-(c) shows the structure of the streamlines, which characterise the flow within the ligament. It is clearly seen that the formation of several stagnation points occurs along the interface reflecting the competition between the capillary- and Marangoni-driven flows an example of which is provided by the stagnation point close to the neck region.

A comparison of the ligament shape between the clean and surfactant-laden cases is shown in Fig. 6, which depicts surface plots of the ligaments together with the magnitude of  $\Gamma$  in the latter case for  $\beta_s = 0.3$ ,  $\Gamma_o = \Gamma_\infty/2$ , and  $Pe_s = 10$  at  $t = 11.11$ . In the presence of surfactant, due to the Marangoni-induced retardation of the retraction process as a result of flow from high- to low-concentration regions, the ligament is longer than in the clean case. Due to the imminent ligament pinchoff for the clean case, higher pressure and velocity fields are observed in comparison to the surfactant-laden case.

In order to separate the effects of mean surface tension and Marangoni stresses, whose magnitude is reduced and enhanced in the presence of surfactant, respectively, we consider an additional ‘clean’ case simulation with a reduced surface tension value (the reduced surface tension is given by Eq. (15) using the initial interfacial concentration). This reflects the (artificial) situation of a retracting, surfactant-covered ligament whose surface tension has been reduced

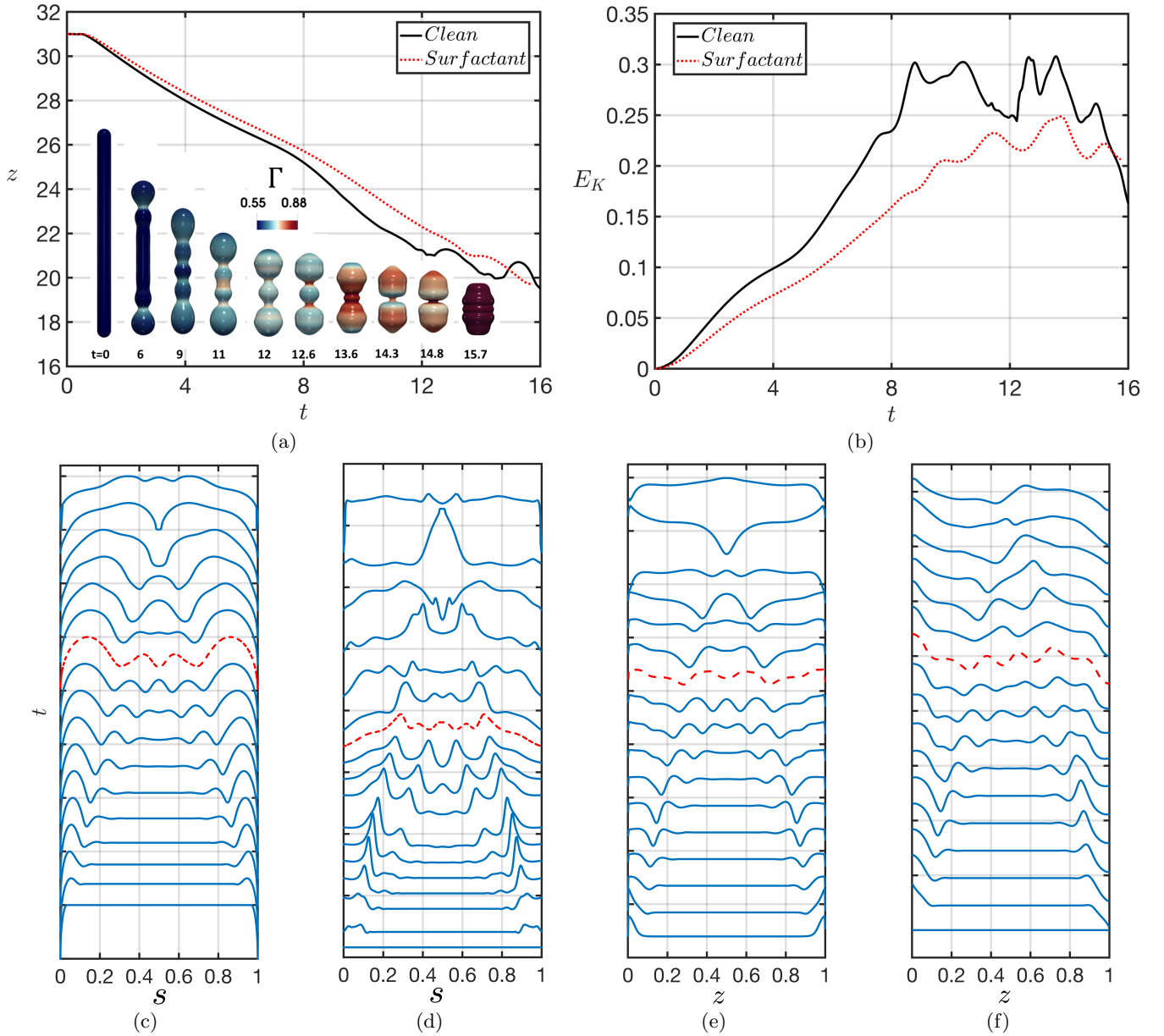


FIG. 4: Ligament retraction with an insoluble surfactant for  $L_o = 15$ ,  $Oh = 10^{-2}$ ,  $Pe_s = 10$ ,  $\beta_s = 0.3$  and  $\Gamma_o = \Gamma_\infty/2$ : (a) temporal evolution of the north tip location for the surfactant-free and surfactant-laden cases, and a three-dimensional representation of the interface for the dimensionless times shown in the panel in which the colour bar depicts the magnitude of the surfactant interfacial concentration,  $\Gamma$ ; (b) temporal evolution of the Kinetic energy  $E_K$  for the surfactant-free and surfactant-laden cases; (c)-(f) time-space plots of the interface,  $\Gamma$ ,  $p$ ,  $u_z$  with snapshots shown between  $t = 0 - 16$  at equal time intervals; here, the red profiles are associated with  $t = 10$ .

but which cannot support Marangoni stresses. Fig. 7 shows that the reduction in surface tension leads to a delay in the ligament retraction but does not prevent breakup; very similar behaviour to the surfactant-free case is observed in terms of the formation of three droplets, which eventually coalesce, and temporal evolution of the kinetic energy which undergoes a slightly delayed rise due to the slower capillary-driven flow, as expected. These results demonstrate that the prevention of the breakup is due to the formation of Marangoni stresses rather than the decrease in surface tension value.

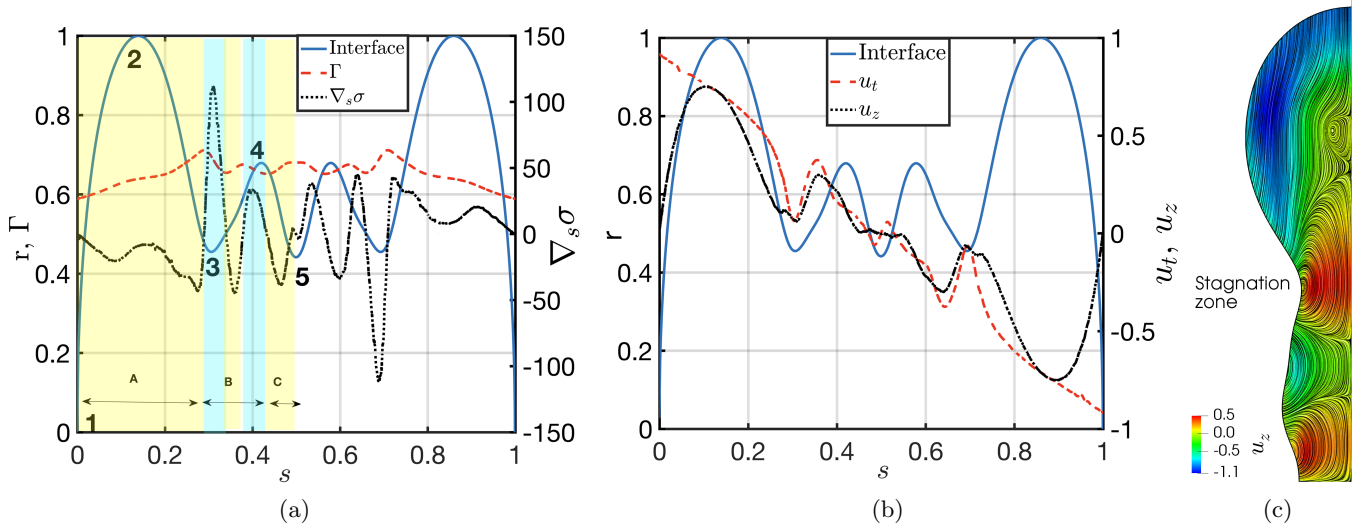


FIG. 5: Spatial variation of the interfacial shape,  $\Gamma$ , and  $\nabla_s \sigma$ , (a), the tangential interfacial velocity,  $u_t$ , for the surfactant-free and surfactant-laden cases, (b), and the streamline structure within the retracting ligament, (c); the parameter values are the same as in Fig. 4 with  $t = 10$ .

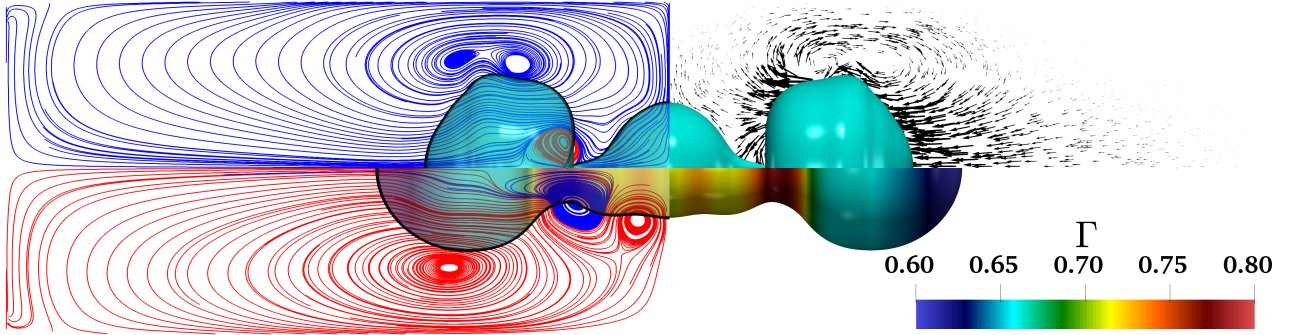


FIG. 6: Comparison of the ligament shapes for the surfactant-free (top) and surfactant-laden (bottom) cases for the same parameters as in Fig. 4 and  $t = 11.11$ . For the surfactant-laden case, the magnitude of  $\Gamma$  is displayed and indicated by the colour bar. Additionally, streamlines (red and blue colour represent counter-clockwise and clockwise rotation, respectively) and a three-dimensional representation of the velocity vector field are also shown.

### C. Parametric study

Here, we investigate the fate of the ligament on system parameters such as the dimensionless elasticity parameter,  $\beta_s$ , the surface Peclet number,  $Pe_s$ , the Biot number,  $Bi$ , and the adsorption parameter,  $x$ . Unless stated otherwise, the parameters remain fixed to their 'base' values:  $L_o = 15$ ,  $Oh = 10^{-2}$ ,  $\beta_s = 0.3$ , and  $Pe_s = 10$ . We shall begin by examining the effect of parameter  $\beta_s$ , which characterises the relative significance of Marangoni stresses. As highlighted above, the redistribution of surfactant along the interface gives rise to concentration gradients and Marangoni stresses that act to retard retraction and prevent ligament pinchoff. Further evidence for this is provided in Fig. 8(a)-(b) in which we plot the temporal evolution of the ligament tip location, and the kinetic energy, respectively, for  $\beta_s = 0.1$  and  $0.5$ . In Fig. 8, we also show a three-dimensional representation of the interface for these  $\beta_s$  values. With increasing  $\beta_s$ , the Marangoni stresses are strengthened leading to a larger reduction in the retraction velocity and highlighting their retarding effect on the dynamics. As can also be seen clearly from Fig. 8(a)-(b), for sufficiently large  $\beta_s$  values, Marangoni stresses dominate the flow preventing ligament breakup. In panels (c) and (e), and (d) and (f) of Fig. 8, in which we plot a snapshot of the interfacial shape,  $\Gamma$ ,  $\nabla_s \sigma$  and  $u_t$  (for the 'clean' and surfactant-laden cases), for  $\beta_s = 0.1$  and  $0.5$ , respectively, it is shown that for the higher  $\beta_s$  value, the larger Marangoni stresses lead to a more uniform distribution of surfactant along the interface and a greater degree of interfacial rigidification; this is illustrated further through the overall reduction in  $u_t$  and  $E_K$  (see Fig. 8(b)) with increasing  $\beta_s$ .

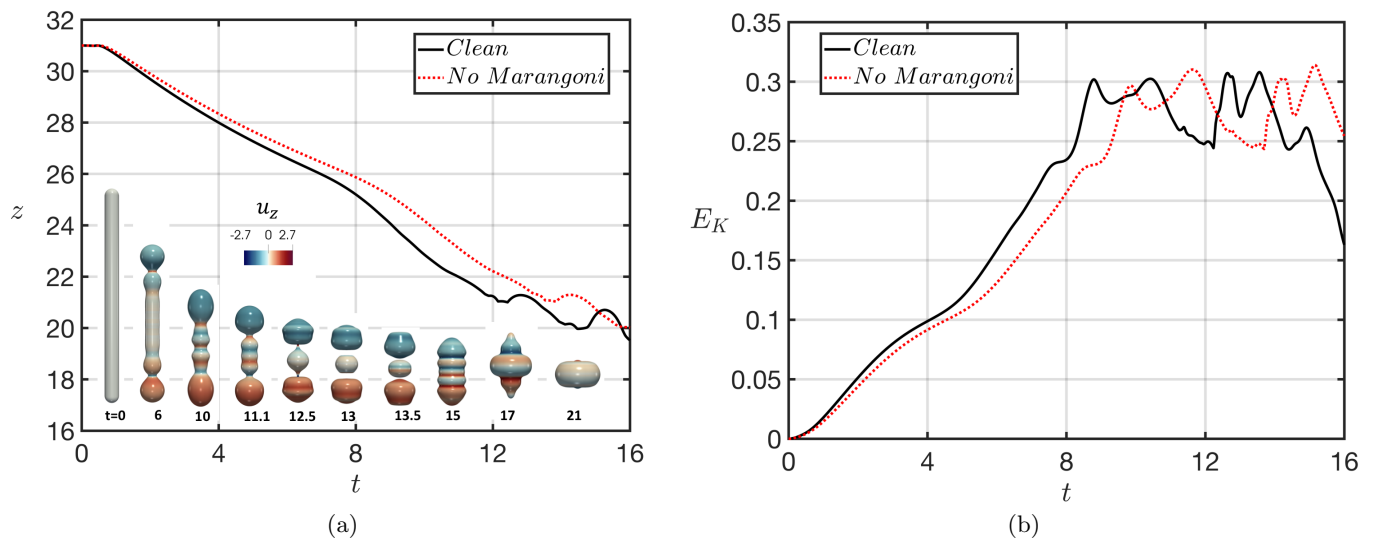


FIG. 7: Dynamics of a retracting, surfactant-covered ligament with isolating the Marangoni effect: (a) temporal evolution of the north tip location for the surfactant-free and surfactant-laden cases, and a three-dimensional representation of the interface for the dimensionless times shown in the panel in which the colour bar depicts the magnitude of the surfactant interfacial concentration,  $\Gamma$ ; (b) temporal evolution of the kinetic energy  $E_K$  for the surfactant-free and surfactant-laden cases.

In Fig. 9, we show the effect of varying  $Pe_s$ , which reflects the influence of surfactant diffusion effects along the interface, on the retraction dynamics. Inspection of this figure reveals that the promotion of diffusive effects through a decrease in  $Pe_s$  leads to a more uniform interfacial distribution of  $\Gamma$  and a reduction in the magnitude of surface tension gradients. It can also be seen that the retraction speed and ligament kinetic energy are weakly-dependent on  $Pe_s$ : they exhibit quantitatively similar dynamics over a three orders of magnitude variation in  $Pe_s$ .

Up to this point, we have only analysed the fate of the ligament in presence of insoluble surfactants; here, we investigate the effect of surfactant solubility on the dynamics by fixing value of the fractional coverage to  $x = 0.9$  and exploring the range  $Bi = 10^{-3} - 1$ . At the lower end of this range, the sorptive time scales are much larger than those associated with interfacial effects; consequently, the dynamics are dominated by capillarity and Marangoni stresses and are expected to be similar to those observed in the insoluble surfactant case. For  $Bi = O(1)$ , the sorptive time scales are comparable to their capillary and Marangoni counterparts and the flow will reflect the delicate interplay amongst these effects. Inspection of Fig. 10-(a) and (b), however, shows that, contrary to expectations,  $Bi$  has a relatively minor effect on the retraction speed and the ligament kinetic energy. From the three-dimensional representations of the interface, it can be seen that the ligament escapes its breakup for all  $Bi$ . For  $Bi = 1$ , we observe the escape from breakup at  $t \sim 12.4$  and  $t \sim 14$ . The radius of the neck prior to its escape also increases with  $Bi$ .

We now investigate the effect of the fractional coverage, represented by  $x$  on the dynamics with  $Bi = 0.1$  and the rest of the parameters set to their ‘base’ values. Fig. 11-(a) and (b) shows that whereas the low  $x$  dynamics resemble that of the surfactant-free case, at high  $x$ , for which adsorption effects are dominant, a significant reduction in the retraction velocity and kinetic energy is observed. Furthermore, as can be seen in Fig. 11-(c) and (f), for large  $x$ , interfacial gradients of the surfactant concentration, and therefore of surface tension, are small, which implies that Marangoni stresses play a minor role in this case. Thus, the reduction in ligament retraction velocity must be related to the significant reduction in the mean value of the surface tension, which acts to diminish the magnitude of capillary effects.

#### D. Vortex breakdown during the retraction

In this section, we highlight the role of the vortical structures, generated inside and outside the ligament, which accompany the retraction process. High values of vorticity are located in the neck region, where the thread radius is small, which is characterised by high curvature values and velocity gradients. During the retraction, there is a large primary vortex due to the filament retraction and a small secondary vortex rotating in the opposite direction. The latter resembles a vortex breakdown type [6, 19, 21, 36, 37] near the neck (as they are depicted by the instantaneous streamlines of Fig. 12-(a) and (b) for the ‘clean’ and surfactant-laden base case, respectively). A vortex breakdown

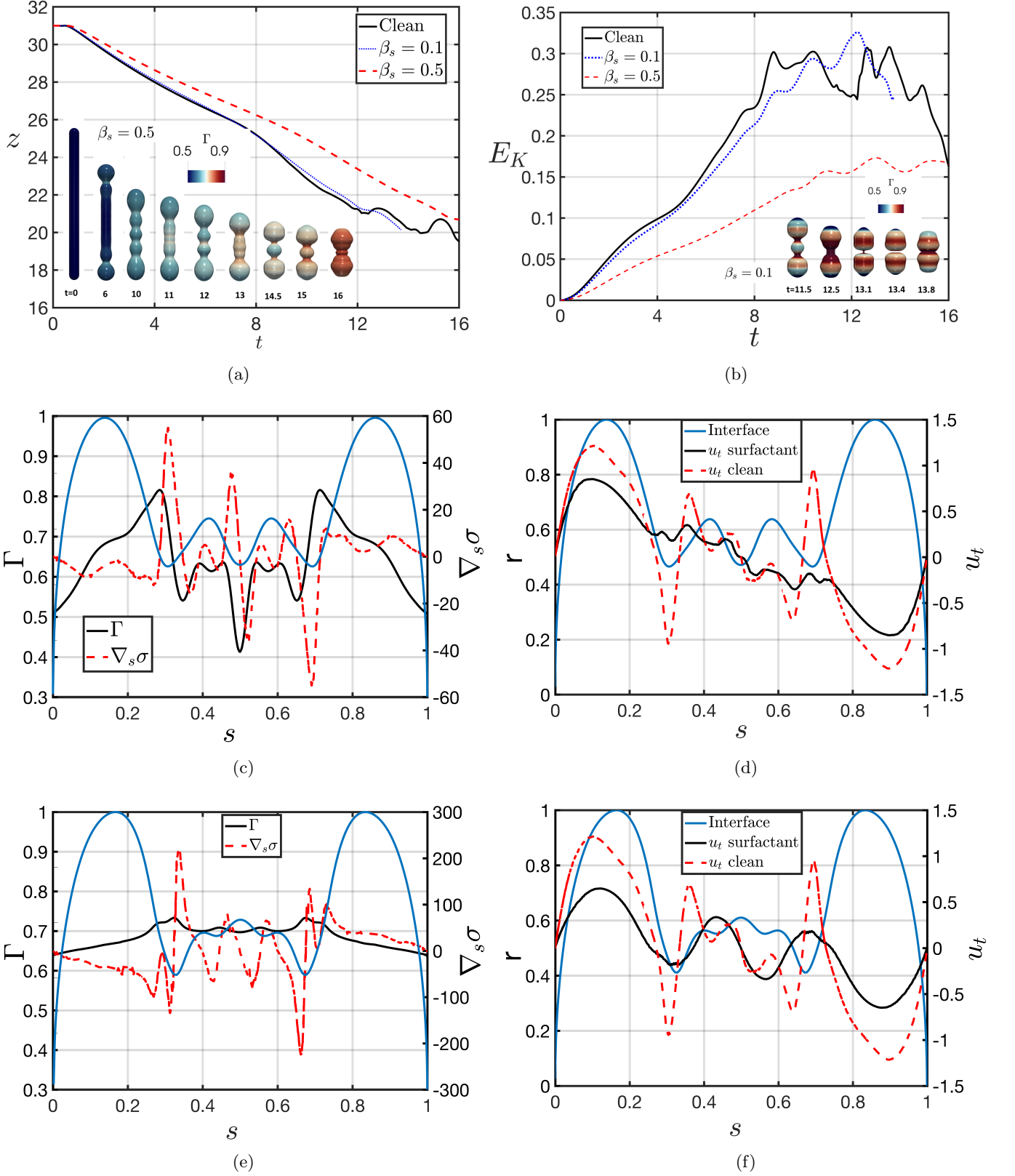


FIG. 8: Effect of  $\beta_s$  on the retraction dynamics for  $L_o = 15$ ,  $Oh = 10^{-2}$ ,  $Pe_s = 10$ , and  $\Gamma_o = x\Gamma_\infty/2$ : (a) and (b) temporal evolution of the north-tip location, and the kinetic energy,  $E_k$ , respectively; (a) and (b) also show three-dimensional representations of the interface for  $\beta_s = 0.5$  and  $0.1$ , respectively, and for the dimensionless times shown in the panels in which the colour bar depicts the magnitude of the surfactant interfacial concentration,  $\Gamma$ .

Panels (c) and (e), and (d) and (f) show the spatial variation of the interfacial shape,  $\Gamma$ , and  $\nabla_s \sigma$ , and the tangential interfacial velocity,  $u_t$ , for the surfactant-free and surfactant-laden cases, respectively, at  $t = 10$ . In (c) and (e), and (d) and (f),  $\beta_s = 0.1$  and  $0.5$ , respectively. Note: in (c) interface location is superimposed, however, axis is not shown.

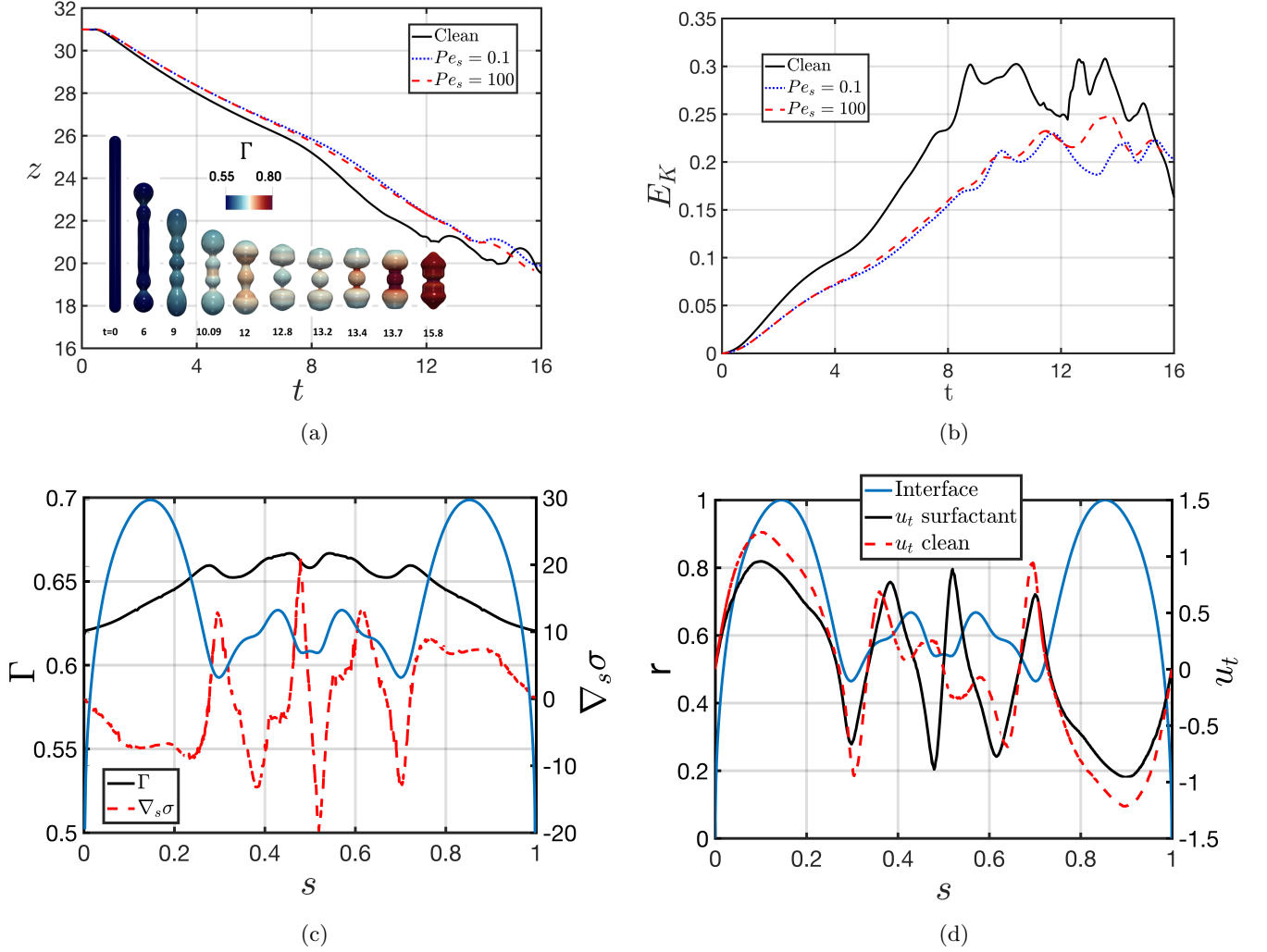


FIG. 9: Effect of  $Pe_s$  on the retraction dynamics for  $L_o = 15$ ,  $Oh = 10^{-2}$ ,  $\beta_s = 0.3$ , and  $\Gamma_o = x\Gamma_\infty/2$ : (a) temporal evolution of the north-tip location and three-dimensional representations of the interface for  $Pe_s = 0.1$  and for the dimensionless times shown in the panels in which the colour bar depicts the magnitude of the surfactant interfacial concentration,  $\Gamma$ ; (b) temporal evolution of the kinetic energy,  $E_k$ . respectively; (a) and (b) also show  $\beta_s = 0.5$  and  $0.1$ , Panels (c) and (d) show the spatial variation of the interfacial shape,  $\Gamma$ , and  $\nabla_s\sigma$ , and the tangential interfacial velocity,  $u_t$ , for the surfactant-free and surfactant-laden cases, respectively, for  $Pe_s = 0.1$  and at  $t = 10$ . Note: in (c) and (d) interface location is superimposed, however, axis is not shown.

refers to stagnation points occurring inside a primary vortex and developing a secondary toroidal circulation. We have chosen these two examples ( $t = 10.9$  for the clean and  $t = 14.6$  for the surfactant-laden base case) because their neck radii have the same size, and for the surfactant case is characterised by the minimum neck radius value before re-opening. We notice that for the clean case, the vortex breakdown occurs inside and outside the neck, and its circulation follows the same direction of neck pinchoff. For the surfactant-laden base case, Marangoni stresses push the vortex breakdown away from the neck, and leads to its re-opening. The variation of the pressure  $p$  and axial velocity component  $u_z$  are also provided for both cases in Fig. 12 highlighting the stagnation point ( $u_z = 0$ ) in the  $z$ -axis.

The example shown in Fig. 12 highlights the vortical structure occurring during a neck pinchoff event for a clean case and neck opening for an insoluble surfactant-laden base case, respectively. However, as shown in Fig. 13, a multitude of vortical structures are formed from the initial stages of retraction until reaching either pinchoff or neck re-opening. Similar structures and behaviour are also observed for soluble surfactant cases. As the ligament retraction is faster for the clean case (see the temporal evolution in Fig. 10-(a)), the pressure and vorticity  $\omega = \nabla \times \mathbf{u}$  are much larger due to the importance of the interface curvature (see Fig. 13-(a), (b) and (c)). Finally, the redistribution of

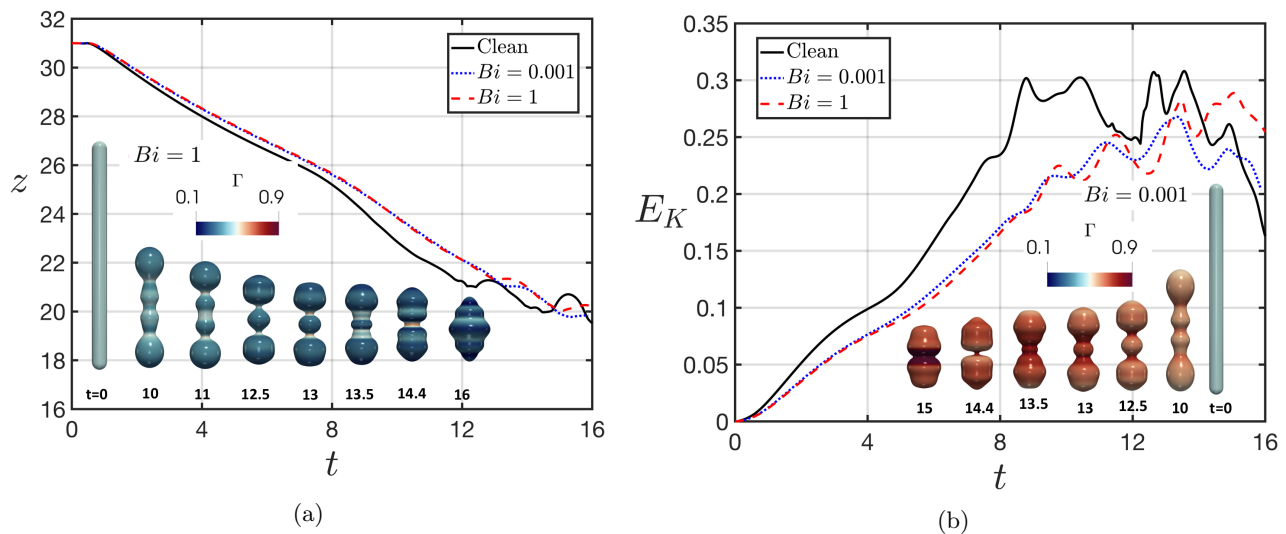


FIG. 10: Effect of  $Bi$  on the retraction dynamics for  $L_o = 15$ ,  $Oh = 10^{-2}$ ,  $\beta_s = 0.3$ ,  $Pe_s = 10$ , and  $\Gamma_o = x\Gamma_\infty/2$ : (a) and (b) temporal evolution of the north-tip location, and the kinetic energy,  $E_k$ , respectively; (a) and (b) also show three-dimensional representations of the interface for  $Bi = 1$  and  $10^{-3}$ , respectively, and for the dimensionless times shown in the panels in which the colour bar depicts the magnitude of the surfactant interfacial concentration,  $\Gamma$ .

Panels (c) and (e), and (d) and (f) show the spatial variation of the interfacial shape,  $\Gamma$ , and  $\nabla_s\sigma$ , and the tangential interfacial velocity,  $u_t$ , for the surfactant-free and surfactant-laden cases, respectively, at  $t = 10$ . In (c) and (e), and (d) and (f),  $Bi = 10^{-3}$  and 1, respectively.

surfactant in the ligament's bulk  $C_\infty$  is shown in Fig. 14. It starts by taking a shape of a mushroom type in the bulbous regions and quasi-constant high concentration in the rest of the ligament thread except in the region adjacent to the interface.

#### IV. CONCLUSIONS

We have presented the effect of surfactant on ligament retraction of an aspect ratio  $L_0 = 15$  and for intermediate Ohnesorge numbers,  $Oh \sim 10^{-2}$ . We have performed fully three-dimensional numerical simulations of the retracting process over a wide range of system parameters that account for the surfactant solubility and sorption kinetics and Marangoni stresses. The numerical method has been validated against the work of Notz and Basaran [26] for a surfactant-free case, and a mesh-refinement study was also performed to ensure that our numerical results are resolution-independent. Our results indicate that the presence of surfactant inhibits ligament breakup and promote neck re-opening through Marangoni-flow, induced by the formation of surfactant concentration gradients, and not via lowering of the mean surface tension. These Marangoni stresses lead to interfacial rigidification, observed through a reduction of the retraction velocity and the ligament kinetic energy.

Future research avenues involve performing numerical simulations of non-Newtonian ligaments, including viscoplastic and visco-elastic types, with a large range of Ohnesorge numbers and ligament aspect ratios.

#### Acknowledgements

This work is supported by the Engineering & Physical Sciences Research Council, United Kingdom, through a studentship in the Centre for Doctoral Training on Theory and Simulation of Materials at Imperial College London funded by the EPSRC (EP/L015579/1) (Award reference:1808927). We acknowledge the Thomas Young Centre under grant number TYC-101. We also acknowledge HPC facilities provided by the Research Computing Service (RCS) of Imperial College London for the computing time.

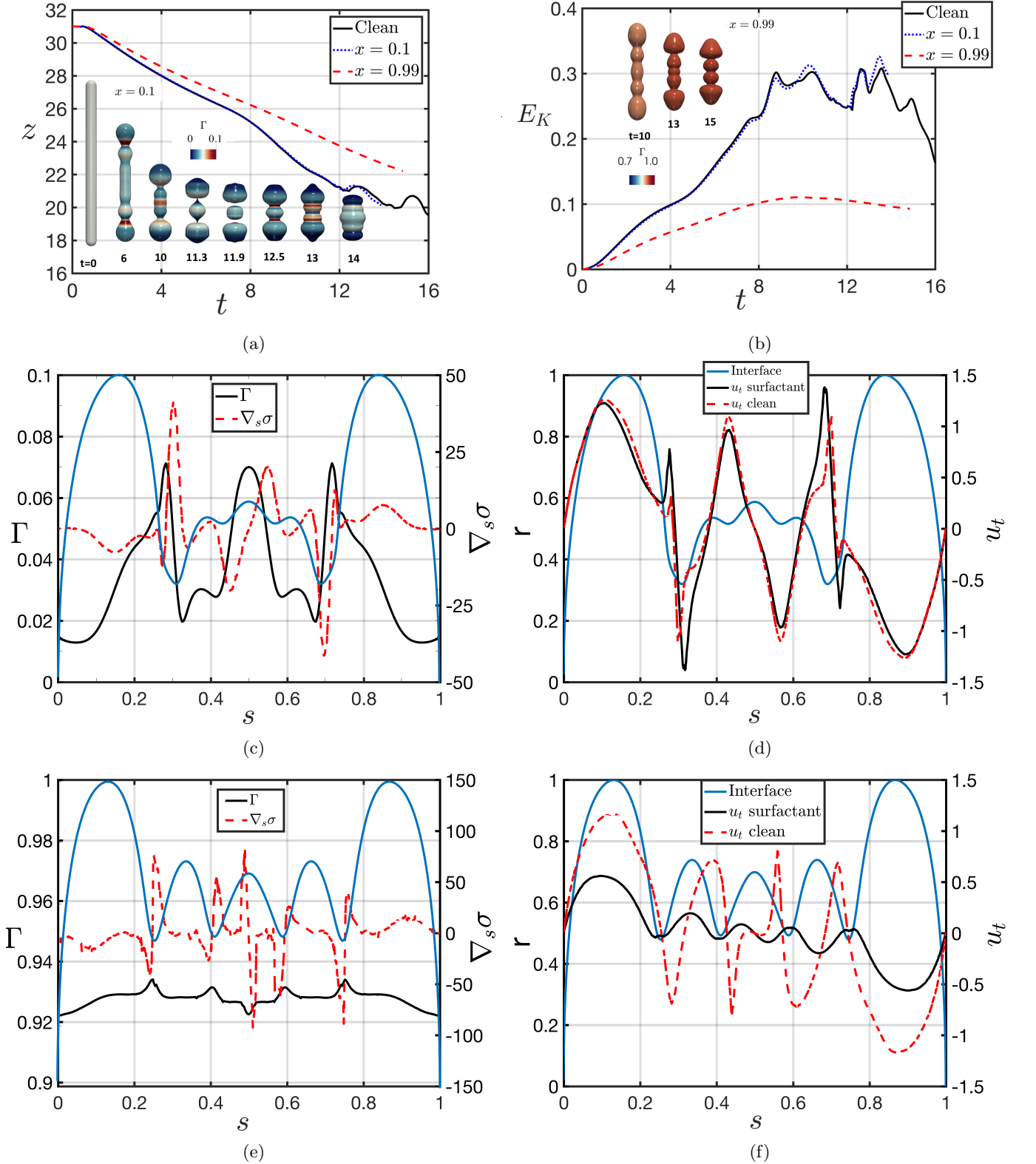


FIG. 11: Effect of  $x$  on the retraction dynamics for  $L_o = 15$ ,  $Oh = 10^{-2}$ ,  $\beta_s = 0.3$ ,  $Pe_s = 10$ , and  $Bi = 0.1$ : (a) and (b) temporal evolution of the north-tip location, and the kinetic energy,  $E_k$ , respectively; (a) and (b) also show three-dimensional representations of the interface for  $x = 0.1$  and  $0.99$ , respectively, and for the dimensionless times shown in the panels in which the colour bar depicts the magnitude of the surfactant interfacial concentration,  $\Gamma$ .

Panels (c) and (e), and (d) and (f) show the spatial variation of the interfacial shape,  $\Gamma$ , and  $\nabla_s \sigma$ , and the tangential interfacial velocity,  $u_t$ , for the surfactant-free and surfactant-laden cases, respectively, at  $t = 10$ . In (c) and (e), and (d) and (f),  $x = 0.1$  and  $0.99$ , respectively. Note: in (c) and (e) interface location is superimposed, however, axis is not shown.

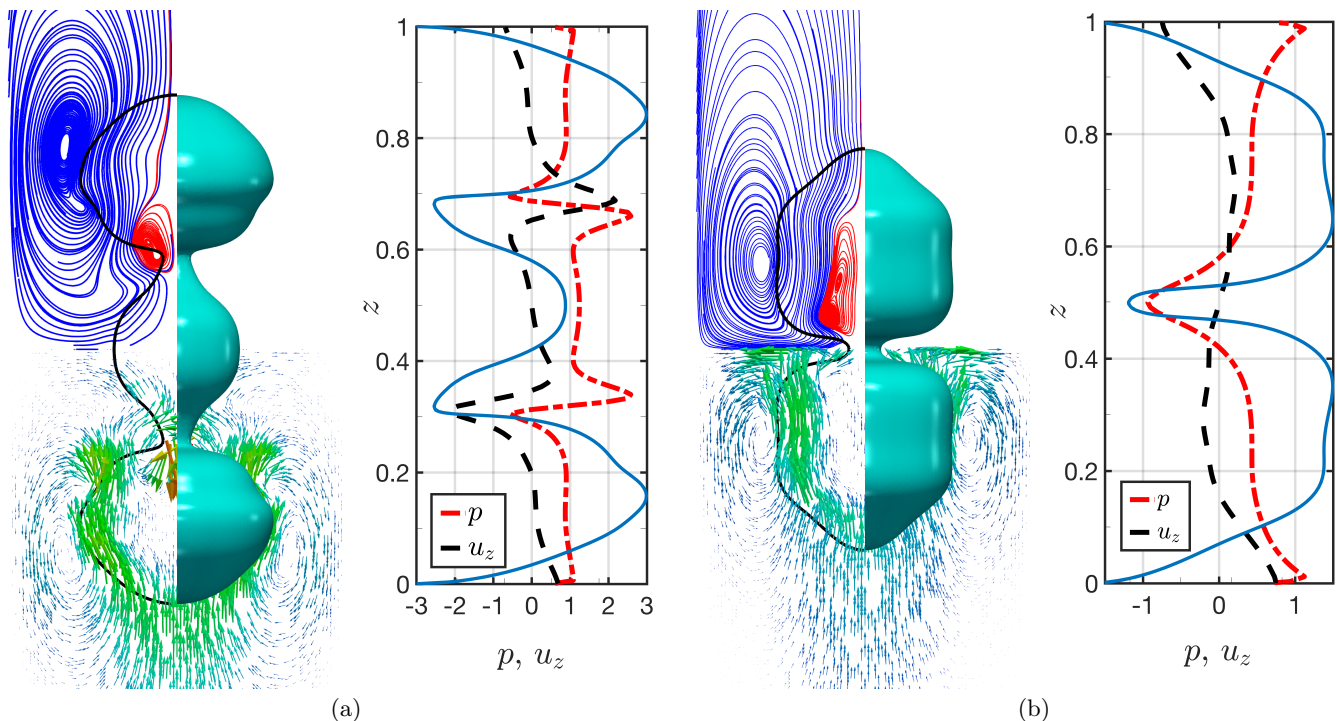


FIG. 12: Effect of surfactant on the vortical structures during ligament retraction: (a) non-surfactant case for  $L_o = 15$ ,  $Oh = 10^{-2}$  at  $t = 10.9$  (b) "base surfactant case" at  $t = 14.6$ . For both cases, transversal slice in the centreline of the domain, with streamlines (top) and the velocity vector field (bottom). Pressure and streamwise velocity in the vertical centreline,  $(0, 0, z)$  is also represented for both cases.

## APPENDIX

In this Appendix, we show that the results presented in this study are mesh-independent. To this end, the dynamics of the retracting ligament ( $L_o = 15$  and  $Oh = 10^{-2}$ ) was tested for different mesh types and their main characteristics are summarised in Table I such as, the number of elements, and the predicted pinchoff time. A M2 mesh-type is formed by around  $\sim 30M$  cells, and M3 mesh-type by  $\sim 230M$  cells. We conclude, that a M2 mesh-type is satisfactory to predict the dynamics regarding ligament retraction, and therefore, all the results presented in this paper corresponds to a M2-mesh type.

TABLE I: Retracting ligament mesh study when  $L_o = 15$  and  $Oh = 10^{-2}$ .

Run	Global mesh size (number of cells)	Number of parallel process threads	Pinchoff time (s)	Total Comput. hours
M1	$96 \times 96 \times 384$	54	11.1151	$\sim 2$
M2	$192 \times 192 \times 768$	432	11.1158	$\sim 70$
M3	$384 \times 384 \times 1536$	432	11.1167	$\sim 288$

- 
- [1] C. R. Anthony, P. M. Kamat, M. T. Harris, and O. A. Basaran, Dynamics of contracting filaments, *Phys. Rev. Fluids*, **4**, 093601 (2019).
- [2] G. Bleys, and P. Joos, Adsorption kinetics of bolaform surfactants at the air/water interface, *The Journ. of Phys. Chem.*, **89**, (6) 1027-1032 (1985).
- [3] O. A. Basaran, Small-scale free surface flows with breakup: Drop formation and emerging applications, *AIChE Journal*, **48**(9), 1842-1848 (2002)
- [4] A. A. Castrejon-Pita, J. R. Castrejon-Pita, and I. M. Hutchings, Breakup of Liquid Filaments, *Phys. Rev. Lett.*, **108**, 074506 (2012)

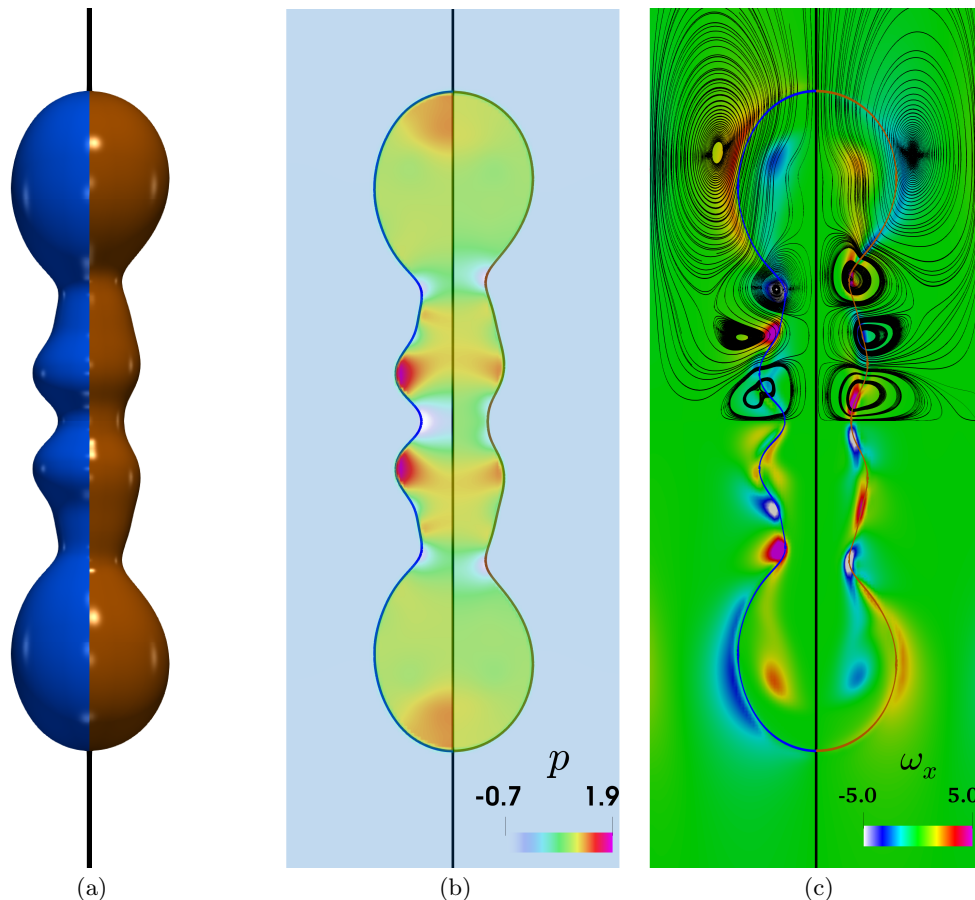


FIG. 13: Different fields at  $t = 10$  for surfactant-free (left) for  $L_o = 15$ ,  $Oh = 10^{-2}$  and soluble surfactant-laden case (right) are  $Pe_s = 10$ ,  $\beta_s = 0.3$ ,  $Bi = 1$ ,  $x = 0.9$  and  $\Gamma_o = \Gamma_\infty/2$ . (a) interface shape; (b) pressure, and (c) vorticity fields.

- [5] R. V. Craster, O. K. Matar, and D. T. Papageorgiou, Pinchoff and satellite formation in surfactant covered viscous threads, *Phys. of Fluids.*, **14**, 1364-1376 (2002)
- [6] O. Daube, Numerical simulation of axisymmetric vortex breakdown in a closed cylinder, in vortex dynamics and vortex methods, *Lectures in Applied Mathematics* Vol. **28**, edited by C. R. Anderson and C. Greengard, pp. 131-152 (American Mathematical Society, 1991)
- [7] R. Day, E. Hinch, and J. Lister, Self-Similar Capillary Pinchoff of an Inviscid Fluid, *Phys. Rev. Lett.*, **80**(4), 704-707 (1998)
- [8] A. Dziedzic, M. Nakrani, B. Ezra, M. Syed, S. Popinet, and S. Afkhami, Breakup of finite-size liquid filaments: Transition from no-breakup to breakup including substrate effects, *Eur. Phys. J. E.*, **42**(19) (2019)
- [9] J. Eggers, Nonlinear dynamics and breakup of free-surface flows, *Rev. Mod. Phys.*, **69**(3), 865-930 (1997)
- [10] J. Eggers, Universal pinching of 3D axisymmetric free-surface flow, *Phys. Rev. Lett.*, **71**(21), 3458-346 (1993)
- [11] J. Eggers, and E. Villermaux Physics of liquid jets, *Rep. Prog. Phys.*, **71**, 036601 (2008)
- [12] J. Hoepffner, and G. Pare Recoil of a liquid filament: escape from pinch-off through creation of a vortex ring, *J. of Fluid Mech.*, **734**, 183197 (2013)
- [13] S. D. Hoath, S. Jung, and I. M. Hutchings A simple criterion for filament break-up in drop-on-demand inkjet printing, *Phys. of Fluids.*, **25**, 021701 (2013)
- [14] A. J. James, and J. Lowengrub. A surfactant-conserving volume-of-fluid method for interfacial flows with insoluble surfactant, *J. Comput. Phys.*, **201**, 68-722, (2004).
- [15] P. Joos, G. Bleys, and G. Petre, Adsorption kinetics of nonanediol and nonane dicarbonic acid at the air/water interface, *Journal de Chimie Physique*, **79**, 387-393 (1982)
- [16] P. Joos, and G. Serrien, Adsorption kinetics of lower alkanols at the air/water interface: Effect of structure makers and structure breakers, *Interface Science*, **127**, (1) 97-103 (1989)
- [17] J. Lister, and H. Stone Capillary breakup of a viscous thread surrounded by another viscous fluid, *Phys. of Fluids*, **10**(11), 2758-2764 (1998)

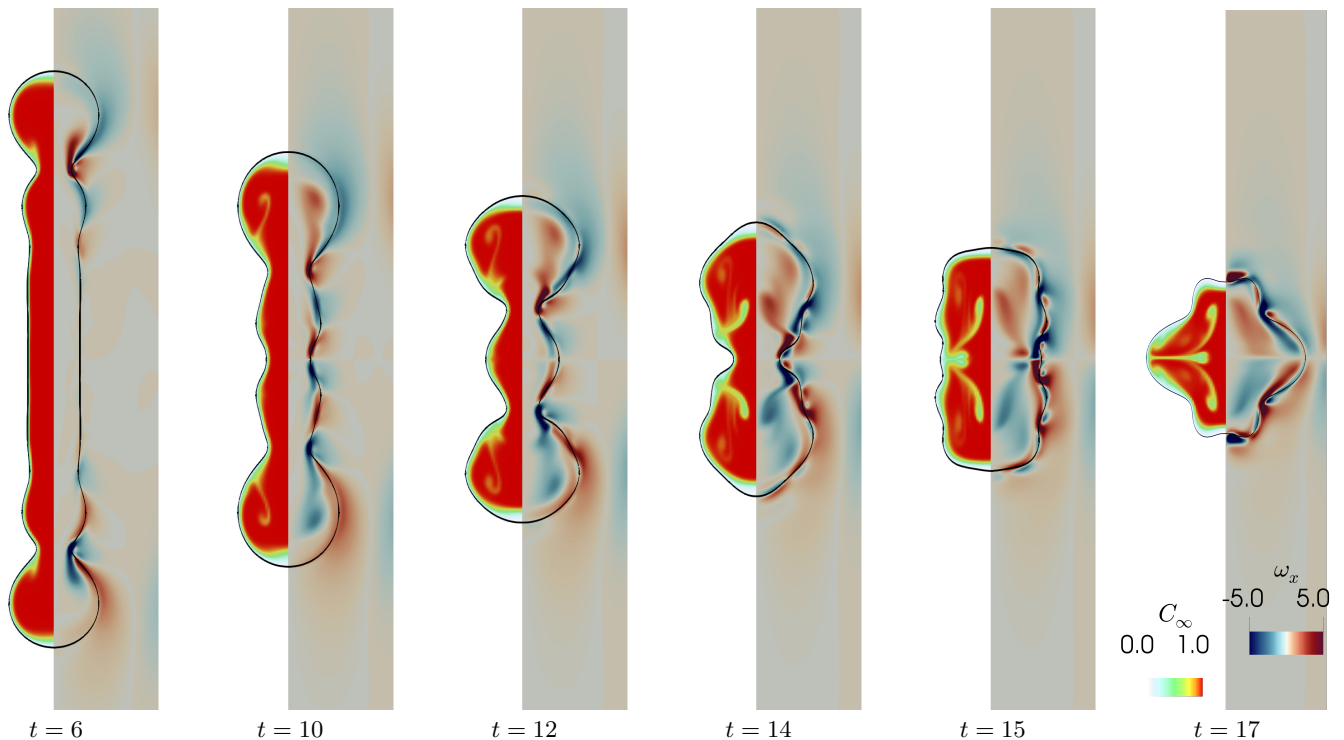


FIG. 14: Spatio-temporal development of the bulk concentration (left) and vorticity (right) for  $L_o = 15$ ,  $Oh = 10^{-2}$ ,  $Pe_s = 10$ ,  $\beta_s = 0.3$ ,  $Bi = 1$ ,  $x = 0.9$  and  $\Gamma_o = \Gamma_\infty/2$ . The surfactant parameters are similar to Fig. 13.

- [18] L. Kahouadji, E. Nowak, J. Kovalchuk, S. Shin, J. Chergui, D. Juric, M. Simmons, R. V. Craster, R. V. and O. K. Matar Simulation of immiscible liquid-liquid flows in complex microchannel geometries using a front-tracking scheme, *Microfluidics and Nanofluidics.*, **22** (11), 126-. (2018)
- [19] L. Kahouadji, and L. Martin Witkowski Free surface due to a flow driven by a rotating disk inside a vertical cylindrical tank: Axisymmetric configuration, *Phys. of Fluids* **26**, 072105 (2014)
- [20] P. M. Kamat, B. W. Wagoner, S. S. Thete, and O. A. Basaran Role of Marangoni stress during breakup of surfactant-covered liquid threads: Reduced rates of thinning and microthread cascades, *Phys. Rev. Fluids.*, **3**(4), 043602 (2018)
- [21] J. M. Lopez, Unsteady swirling flow in an enclosed cylinder with reflectional symmetry, *Phys. Fluids* **7**, 2700?2714 (1995)
- [22] P. Marmottant, and E. Villermaux, On spray formation, *J. of fluid mech.*, **498**, 73-111, (2004)
- [23] P. T. McGough, and O. B. Basaran Repeated Formation of Fluid Threads in Breakup of a Surfactant-Covered Jet, *Phys. Rev. Lett.*, **96**(5), 054502 (2006)
- [24] M. Muradoglu and G. Tryggvason, A front-tracking method for computation of interfacial flows with soluble surfactants, *J. Comput. Phys.*, **227**, 2238-2262 (2008)
- [25] M. Muradoglu and G. Tryggvason, Simulation of soluble surfactants in 3D multiphase flow, *J. Comput. Phys.* **274**, 737-757 (2014).
- [26] P. Notz, and O. A. Basaran Dynamics and breakup of a contracting liquid filament, *J. of Fluid Mech.*, **512**, 223-256 (2004)
- [27] J. A. F. Plateau, Experimental and Theoretical Statics of Liquids Subject to Molecular Forces Only, *Gauthier-Villars: Paris* (1873)
- [28] C. S. Peskin, Numerical analysis of blood flow in the heart, *J. Comp. Phys.* **25** 220-252 (1977).
- [29] L. Rayleigh, On the capillary phenomena of jets, *Proc. London Math. Soc.* **29**, 71-97 (1879)
- [30] R. M. S. M Schulkes, The contraction of liquid filaments, *J. of Fluid Mech.* **309**, 277-300 (1996)
- [31] S. Shin, J. Chergui, D. Juric, L. Kahouadji, O. K. Matar, and R. V. Craster, An Interface-Tracking Technique for Multiphase Flow with Soluble Surfactant, *J. of Comp. Physics*, **359**, 409 - 435 (2018)
- [32] S. Shin, and D. Juric, High order level contour reconstruction method, *J. of Mech. Sc. and Tech.*, **21** (2), 311-326 (2007)
- [33] S. Shin, J. Chergui, and D. Juric, A solver for massively parallel direct numerical simulation of three-dimensional multiphase flows, *J. of Mech. Sc. and Tech*, **31**, 1739-175 (2017)
- [34] S. Shin, D. Juric, S. Abdel-Khalik, and V. Daru, Accurate representation of surface tension using the level contour reconstruction method, *J. of Comp. Physics*, **203** (2), 493 - 516 (2005)
- [35] S. Shin, and D. Juric, Modelling Three-Dimensional Multiphase Flow Using a Level Contour Reconstruction Method for Front Tracking without Connectivity, *J. of Comp. Physics.*, **180** (2), 427 - 470 (2002)
- [36] A. Spohn, M. Mory, and E. Hopfinger, Observations of vortex breakdown in an open cylindrical container with a rotating bottom, *Exp. Fluids* **14**, 70-77 (1993)

- [37] A. Spohn, M. Mory, and E. Hopfinger, Experiments on vortex breakdown in a confined flow generated by a rotating disc, *J. Fluid Mech.* **370**, 73-99 (1998).
- [38] K. E. Teigen, P. Song, J. Lowengrub, and A. Voigt, A diffuse-interface method for two-phase flows with soluble surfactants, *J. Comput. Phys.* **230**, 375-393 (2011).
- [39] Q. Xu, Y. C. Liao, and O. A. Basaran, Can Surfactant Be Present at Pinch-Off of a Liquid Filament?, *Phys. Rev. Lett.*, **98**, 054503 (2007)
- [40] Q. Xu, Computational and theoretical analysis of Ink-jets drop formation and breakup, *PhD Thesis.*, Purdue University. (2007)
- [41] A. A. Wang, C. G. Bailey, W. Wang, and Y. Sui, A fate-alternating transitional regime in contracting liquid filaments, *J. of Fluid Mech.* **860**, 640-653 (2019)